

# Hierarchically-Structured NiO Nanoplatelets as Mesoscale p-Type Photocathodes for Dye-Sensitized Solar Cells

Cory J. Flynn,<sup>†</sup> EunBi E. Oh,<sup>†</sup> Shannon M. McCullough,<sup>†</sup> Robert W. Call,<sup>‡</sup> Carrie L. Donley,<sup>§</sup> Rene Lopez,<sup>‡</sup> and James F. Cahoon<sup>\*,†</sup>

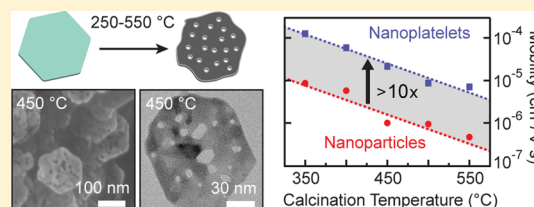
<sup>†</sup>Department of Chemistry, University of North Carolina at Chapel Hill, Chapel Hill, North Carolina 27599-3290, United States

<sup>‡</sup>Department of Physics and Astronomy, University of North Carolina at Chapel Hill, Chapel Hill, North Carolina 27599-3255, United States

<sup>§</sup>Chapel Hill Analytical and Nanofabrication Laboratory (CHANL), Department of Applied Physical Sciences, University of North Carolina at Chapel Hill, Chapel Hill, North Carolina 27599-3216, United States

## S Supporting Information

**ABSTRACT:** A p-type metal oxide with high surface area and good charge carrier mobility is of paramount importance for development of tandem solar fuel and dye-sensitized solar cell (DSSC) devices. Here, we report the synthesis, hierarchical morphology, electrical properties, and DSSC performance of mesoscale p-type NiO platelets. This material, which exhibits lateral dimensions of 100 nm but thicknesses less than 10 nm, can be controllably functionalized with a high-density array of vertical pores 4–6, 5–9, or 7–23 nm in diameter depending on exact synthetic conditions. Thin films of this porous but still quasi-two-dimensional material retain a high surface area and exhibit electrical mobilities more than 10-fold higher than comparable films of spherical particles with similar doping levels. These advantages lead to a modest, 20–30% improvement in the performance of DSSC devices under simulated 1-sun illumination. The capability to rationally control morphology provides a route for continued development of NiO as a high-efficiency material for tandem solar energy devices.



## 1. INTRODUCTION

DSSCs have been pursued as a low-cost solar energy platform for more than two decades. The most well-developed dye-sensitized devices exhibit power-conversion efficiencies above 12% and use TiO<sub>2</sub> as a mesoporous photoanode.<sup>1</sup> In the typical configuration, the TiO<sub>2</sub> surface is functionalized with molecular chromophores that inject electrons into the material, and the oxidized chromophore is regenerated by a liquid electrolyte. More recently, dye-sensitized photoelectrosynthesis cells (DSPECs) have been developed using a similar device configuration but replacing the chromophore with a chromophore–catalyst assembly that can catalyze redox processes for solar fuels generation.<sup>2,3</sup> Despite the success of both DSSC and DSPEC devices using TiO<sub>2</sub> photoanodes, future devices are likely to require a tandem configuration composed of both photoanode (e.g., TiO<sub>2</sub>) and photocathode materials.<sup>4,5</sup> Tandem devices can produce the larger photopotentials that are needed to generate solar fuels;<sup>6</sup> however, initial efforts to create these devices have yielded poor performance primarily limited by the photocathode material.<sup>7,8</sup>

Development of an optically transparent and high-performance p-type photocathode is a long-standing problem. Most development efforts have focused on metal oxides because of their generally large band gaps and low cost. Although several delafossite materials (CuMO<sub>2</sub>; M = Al, Ga, Cr) have been considered,<sup>9–12</sup> NiO is the most well-developed and to-date

highest performance wide-band-gap p-type metal oxide with a record photoconversion efficiency of 1.3% in a DSSC configuration.<sup>13</sup> This material generally exhibits low power-conversion efficiencies in DSSC devices even when using optimized molecular chromophores with a donor–acceptor structure that enhances charge separation and reduces recombination.<sup>14–17</sup> There are several interrelated reasons for the low performance of NiO devices,<sup>18,19</sup> including low hole mobility, poor chromophore surface loading, high charge carrier recombination rates, and a low dielectric constant. Here, we attempt to address a subset of these problems by rationally controlling the morphology and microstructure of the material.

Although mesoporous nanoparticle films are beneficial for surface area, the high density of interparticle boundaries is generally detrimental to electrical characteristics. For instance, mobility values of 0.53 cm<sup>2</sup>/V·s have been reported for bulk NiO films<sup>20</sup> whereas nanoparticle films have values at least 5 orders of magnitude lower, ranging from 5 × 10<sup>−7</sup> to 6 × 10<sup>−6</sup> cm<sup>2</sup>/V·s.<sup>18,21</sup> This effect has driven interest in alternative morphologies, such as nanowires,<sup>22</sup> for metal oxides, which could improve electrical conduction by decreasing charge carrier hopping and scattering at defects and boundaries.

**Received:** March 20, 2014

**Revised:** June 5, 2014

**Published:** June 6, 2014

Recently, mesoporous  $\text{TiO}_2$  single crystals have been synthesized that preserve high surface area but permit electrical conduction through large crystalline regions of the material.<sup>23</sup> For  $\text{TiO}_2$ , this strategy resulted in an increase in the effective charge carrier mobility by approximately 1 order of magnitude,<sup>23</sup> and a similar effect was observed for crystals of  $\text{Fe}_2\text{O}_3$ .<sup>24</sup> Here, we present a first step toward developing new, more efficient morphologies for NiO and designing thin films that can be used in tandem DSSC and DSPEC solar energy devices.

## 2. MATERIALS AND METHODS

**2.1. Materials and Reagents.** Acetonitrile (99.6%), terpineol (anhydrous), Coumarin-343 (97%), ethyl cellulose (viscosity 300 cP), guanidine thiocyanate (>99%), iodine (>99.99%), lithium perchlorate (>99%), nickel nitrate hexahydrate (99.999%), sodium hydroxide (>97%), 4-*tert*-butylpyridine (96%), and valeronitrile (99.5%) were all purchased from Sigma-Aldrich. Methyl methacrylate (MMA) and poly(methyl methacrylate) (PMMA) were purchased from Microchem. Ammonium hydroxide, absolute ethanol (Decon Laboratories), hydrochloric acid (technical grade), and isopropyl alcohol (IPA; electronics grade) were purchased from Fisher Scientific. 1,3-Dimethylimidazolium iodide and 25  $\mu\text{m}$  thick Surlyn polymer were purchased from Solaronix. Spherical NiO nanoparticles (size  $\approx 20$  nm and surface area  $> 50$   $\text{m}^2/\text{g}$ ) were obtained from Inframat Advanced Materials (product 28N-0801); this product has been widely used for p-type DSSC devices.<sup>8,13,16</sup> All chemicals were used as received. Fluorine-doped tin oxide (FTO) glass was purchased from Hartford glass and cleaned with typical organic solvents and sonication.

**2.2. Synthesis of NiO Nanoplatelets.** Synthesis of ultrathin, hexagonal nanoplatelets was adapted from Matjiveć.<sup>25</sup> To a refluxing aqueous solution of 0.01 M  $\text{Ni}(\text{NO}_3)_2$ , a stoichiometric volume of 1.0 M  $\text{NH}_4\text{OH}$  was added and refluxed for 2 h before the colloidal solution was allowed to cool to room temperature. The colloid settled over 1–2 days, the supernatant was decanted, and the resulting concentrated colloid was filtered and dried at 40  $^\circ\text{C}$ . Powder samples were then prepared by calcining dried colloid in an open-air furnace at the desired temperature for 40 min (10 min ramp, 30 min hold). Room humidity was noted to be  $<20\%$ .

**2.3. NiO Paste Preparation.** A viscous paste, using a modification of literature procedures,<sup>8</sup> was made by dispersing 16 g of the dried  $\text{Ni}(\text{OH})_2$  powder into 110 mL of ethanol with mild sonication and vigorous stirring. A 100 mL amount of  $\alpha$ -terpineol was gently heated with stirring to 70  $^\circ\text{C}$  followed by addition of 4.6 g of ethyl cellulose over the course of 30 min. The viscous ethyl cellulose/ $\alpha$ -terpineol solution was then cooled to room temperature. Solutions were combined and allowed to stir overnight. Ethanol was removed by rotary evaporation over the course of 2 h yielding a highly viscous paste. The paste was then rediluted with ethanol to a desired viscosity. Films were spin cast (Laurel WS-650MZ-23NPP) onto FTO glass to yield  $\sim 1$ – $3$   $\mu\text{m}$  thick films and annealed/calcined in an open-air furnace for 40 min (10 min ramp, 30 min hold) at the desired temperature. For preparation of films with spherical nanoparticles, commercial NiO powder (Inframat) was substituted for  $\text{Ni}(\text{OH})_2$  nanoplatelet powder. All subsequent paste preparation, film deposition, and DSSC fabrication procedures were identical for the two materials.

**2.4. Analytical Methods.** Powder X-ray diffraction (XRD) experiments were performed on a Rigaku Multiflex from 10 $^\circ$  to

100 $^\circ$   $2\theta$  at a scan rate of 2 $^\circ$   $2\theta/\text{min}$  unless otherwise stated. XRD patterns were normalized to their highest peak intensity. Brunauer–Emmett–Teller (BET) surface area measurements were conducted utilizing a home-built system at  $\sim 77$  K with  $\text{N}_2$  gas. Film thickness measurements were conducted with a KLA Tencor P-6 stylus profilometer. High-resolution transmission electron microscopy (TEM) was performed on a JEOL 2010F-FasTEM using a 200 kV accelerating voltage. Selected-area electron diffraction (SAED) patterns were obtained using apertures smaller than the  $\sim 100$  nm particle size and thus represent diffraction from within an individual grain, unless stated otherwise. Scanning electron microscopy (SEM) imaging was performed on a FEI Helios NanoLab DualBeam D600 with powder samples deposited on carbon tape. X-ray photoelectron spectroscopy (XPS) measurements were performed with a Kratos Axis Ultra DLD X-ray photoelectron spectrometer with ultraviolet photoelectron spectroscopy (UPS) capability, and all XPS data was corrected to the C 1s peak at 284.6 eV. For XPS data, the O 1s region was fit to a sum of three Voigt functions (70/30 Gaussian/Lorentzian) centered at  $\sim 529.2$ ,  $\sim 530.9$ , and  $\sim 531.6$  eV. Electronic absorption measurements were acquired with a Cary 5000 UV–vis–NIR from Agilent with integrating sphere attachment. Mott–Schottky measurements were performed in standard 0.2 M  $\text{LiClO}_4$  at pH 5.8 (adjusted with  $\text{HClO}_4$  and  $\text{NaOH}$  as needed) in a three-electrode configuration (working, NiO on FTO; counter, Pt wire; reference,  $\text{Ag}/\text{AgCl}$ ) with a Gamry Reference 600 electrochemical impedance spectrometer at 500 and 1000 Hz utilizing a standard series RC equivalent circuit. The linear portion of the  $1/C^2$  decay was then fit with a linear function yielding  $R^2 > 0.98$ . The projected area of the electrode was utilized in order to extract an upper limit of doping level, which corresponds to a lower limit of carrier mobility.

**2.5. Microelectrode Fabrication and Conductivity Measurements.** Standard electron-beam lithography using MMA/PMMA was performed using a Hitachi S4700 SEM. Cr/Au (3/50 nm) was deposited using thermal evaporation (KEY KV-301). A NiO paste was spin cast on the electrodes and annealed as desired. Electrical measurements were performed with a Keithley 2636A SourceMeter in conjunction with Signatone micropositioners (S-725) and probe tips (SE-TL). Measured NiO conductance values did not depend on the contacting probe geometry, confirming the electrical uniformity of the Au films after high-temperature annealing.

**2.6. DSSC Fabrication and Electrical Characterization.** NiO films were immersed directly after annealing in 0.1 mM ethanolic Coumarin-343 overnight, rinsed with IPA, and dried with  $\text{N}_2$ . Pt counter electrodes were fabricated by thermal decomposition of 5 mM  $\text{H}_2\text{PtCl}_6$  in IPA onto FTO glass at 380  $^\circ\text{C}$  for 30 min. The platinized counter electrode was sandwiched with the working electrode with a 25  $\mu\text{m}$  Surlyn gasket in a custom-made heating press. Z960-like electrolyte (1.0 M 1,3-dimethylimidazolium iodide, 0.03 M iodine, 0.5 M *tert*-butylpyridine, and 0.1 M guanidium thiocyanate in an 85/15 (v/v) acetonitrile/valeronitrile) was vacuum backfilled using a vacuum chamber apparatus. The cell was then sealed with Surlyn film and a microscope coverslip. Current–voltage curves were obtained under AM1.5G illumination using a Newport Oriel 150W Class ABB Solar Simulator that was calibrated to 1-sun intensity using a certified reference solar cell (Newport 91150 V). Electrical measurements were performed with a Keithley 2636A SourceMeter.

### 3. RESULTS AND DISCUSSION

Ultrathin, hexagonal  $\text{Ni}(\text{OH})_2$  platelets, as shown in SEM images in Figure 1A, are highly uniform with a facet-to-facet lateral distance of  $102 \pm 15$  nm and thickness of 8–10 nm. Hydroxide platelets were converted to NiO by calcination in air at temperatures ranging from 250 to 600 °C. As illustrated schematically in Figure 1B, calcination generally preserved the hexagonal cross section and dimensions of the platelets. Surprisingly, we also observed formation of pores in the material. SEM images (see Figure 1C) show progressively larger pores at higher calcination temperatures, producing average pore sizes of  $5 \pm 1$ ,  $7 \pm 2$ , and  $15 \pm 8$  nm at 350, 450, and 550 °C, respectively. Similar high-porosity NiO plates were recently reported for application in supercapacitors,<sup>26</sup> and this type of nanoscale pore formation has been observed during crystallization of 15 nm thick amorphous Si films.<sup>27</sup> Pore formation is presumed to be mechanically driven by the 2-fold increase in density upon conversion from  $\text{Ni}(\text{OH})_2$  to NiO. Temperatures of 600 °C and greater caused sintering of the NiO particles and loss of all pore structure, as evident from the SEM image in the right-hand panel of Figure 1C.

XRD on powders of  $\text{Ni}(\text{OH})_2$  that had been processed at temperatures from 100 to 600 °C (Figure 2A) showed conversion to NiO at a threshold temperature of 250 °C. Line widths in the XRD spectra progressively narrow at higher calcination temperatures, and analysis using the Debye–Scherrer equation (see Figure S1, Supporting Information) indicates an increase in the crystallite grain size from 9 to 15 nm at 250–400 °C to from 18 to 25 nm at 500–600 °C. Considering the 100 nm lateral dimension of the particles, this analysis suggests the individual hexagonal particles are polycrystalline with a relatively large grain size even at low temperatures, which is confirmed by TEM analysis (see below).

The temperature-induced changes in morphology and crystallinity were accompanied by a dramatic change in the color, as shown in Figure 2B. The color of powders varied from bright green for  $\text{Ni}(\text{OH})_2$  to black and light gray for low-temperature and high-temperature NiO, respectively. The dark color of NiO is typically attributed to the presence of  $\text{Ni}^{3+}$  impurity centers, which give rise to  $\text{Ni}^{2+}$ – $\text{Ni}^{3+}$  intervalence charge-transfer transitions in the visible wavelength range.<sup>28</sup>

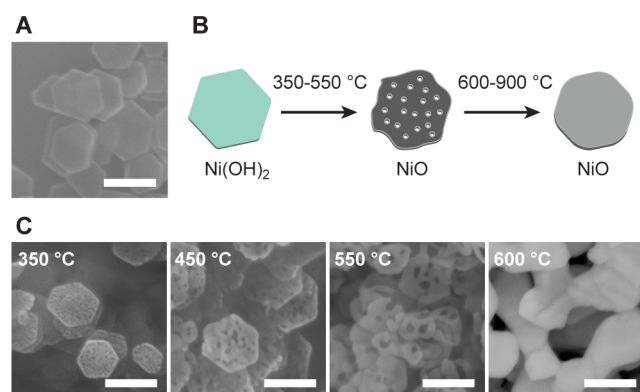


**Figure 1.** Morphology of  $\text{Ni}(\text{OH})_2$  and NiO nanoplatelets. (A) SEM image of as-synthesized  $\text{Ni}(\text{OH})_2$  platelets; scale bar, 100 nm. (B) Schematic of the conversion between  $\text{Ni}(\text{OH})_2$  and NiO at varying temperatures. (C) SEM images of NiO formed from calcination in air of  $\text{Ni}(\text{OH})_2$  platelets at the temperature denoted in the upper-left corner of each image; all scale bars, 100 nm.

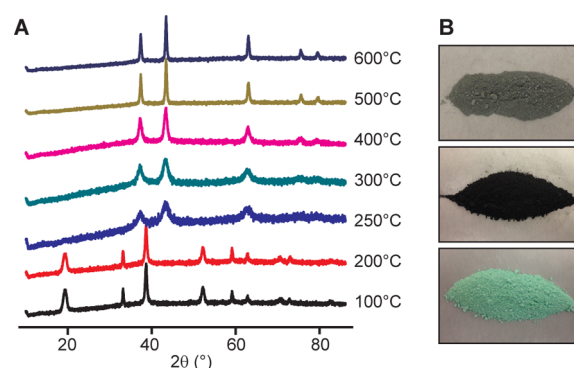


**Figure 2.** Crystallinity and color of NiO nanoplatelets. (A) Powder XRD spectra for  $\text{Ni}(\text{OH})_2$  or NiO platelets processed at the temperature denoted to the right of each spectrum. (B) Photographs of  $\text{Ni}(\text{OH})_2$  (bottom) and NiO formed at 450 (middle) and 600 °C (top).

The  $\text{Ni}^{3+}$  centers are also associated with Ni vacancies that produce the p-type conductivity of the material.<sup>29</sup> Although recent reports<sup>30</sup> have suggested the dark color may indicate the presence of  $\text{Ni}^0$ , we found no evidence (see Figure S2, Supporting Information) to support the presence of  $\text{Ni}^0$  in the platelets.

To further elucidate the morphology of the NiO platelets, we performed high-resolution TEM imaging on a series of samples. Imaging of the  $\text{Ni}(\text{OH})_2$  platelets (Figure 3A) shows a uniform and crystalline material, and SAED patterns yield a hexagonal pattern expected from  $\beta$ - $\text{Ni}(\text{OH})_2$ . Lattice-resolved imaging on the side of a platelet (Figure 3A, right) shows fringes spaced by 4.4–4.8 Å, which is in good agreement with the expected spacing of 4.6 Å along the  $\langle 001 \rangle$  direction.<sup>31</sup>

TEM imaging of a sample calcined at 250 °C (Figure 3B, left) confirms the presence, even at this low temperature, of a

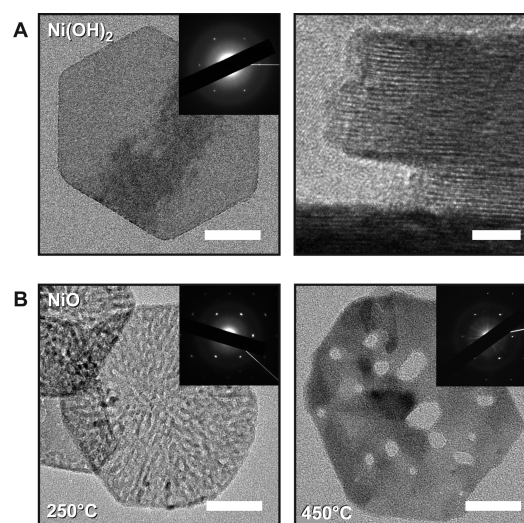


**Figure 3.** TEM images and SAED patterns showing the morphology and crystallinity of nanoplatelets. (A) (Left) TEM image of a single  $\text{Ni}(\text{OH})_2$  platelet; scale bar, 30 nm. (Inset) SAED pattern from a single grain of the platelet. (Right) Side-on TEM image of a  $\text{Ni}(\text{OH})_2$  platelet; scale bar, 5 nm. (B) (Left) TEM image of a NiO platelet calcined at 250 °C; scale bar, 30 nm. (Inset) SAED pattern from a single grain of the platelet. (Right) TEM image of a NiO platelet calcined at 450 °C; scale bar, 30 nm. (Inset) SAED pattern from a single grain of the platelet.



high density of pores that are 2–3 nm in diameter. SAED patterns collected from a single platelet show a pattern consistent with the  $[111]$  direction of the cubic phase of NiO, indicating conversion of the (001) face of  $\beta$ -Ni(OH)<sub>2</sub> to the (111) face of NiO. TEM imaging of NiO calcined at 450 °C (Figure 3B, right) shows formation of larger pores that clearly extend through the entire platelet. SAED again confirms the cubic phase of NiO oriented in the  $[111]$  direction, and additional SAED patterns of this 450 °C sample (see Figure S3, Supporting Information) indicate that the individual particles contain a small number of twist grain boundaries. TEM analysis combined with the temperature-dependent XRD data in Figure 2A suggest that individual NiO nanoplatelets are polycrystalline but contain a decreasing number of crystal grains per particle with increasing calcination temperatures.

High surface area metal oxide films for DSSCs are typically composed of randomly oriented spherical nanoparticles 5–20 nm in diameter. In contrast, films of the NiO platelets produce a high-density array partially oriented in the  $[111]$  direction, as evident from the SEM image of a characteristic film in Figure 4A and additional images in Figure S4, Supporting Information.<sup>32</sup> To explore the electrical characteristics of these films, we measured the lateral conductivity of NiO films using microfabricated Au electrodes, as depicted in Figure 4B. The average resistances of platelet and nanoparticle films prepared under identical conditions and annealed at 450 °C are plotted as a function of electrode separation in Figure 4C. Resistance values from the nanoparticle films are 10–100-fold larger than values from the platelets. A linear fit of the data yields conductivities of  $(6 \pm 1) \times 10^{-5} \text{ S}\cdot\text{cm}^{-1}$  and  $(2.2 \pm 0.8) \times 10^{-3} \text{ S}\cdot\text{cm}^{-1}$  for particles and platelets, respectively, using film thicknesses measured by profilometry. We performed similar measurements over a range of annealing temperatures, and the conductivity values as a function of temperature are

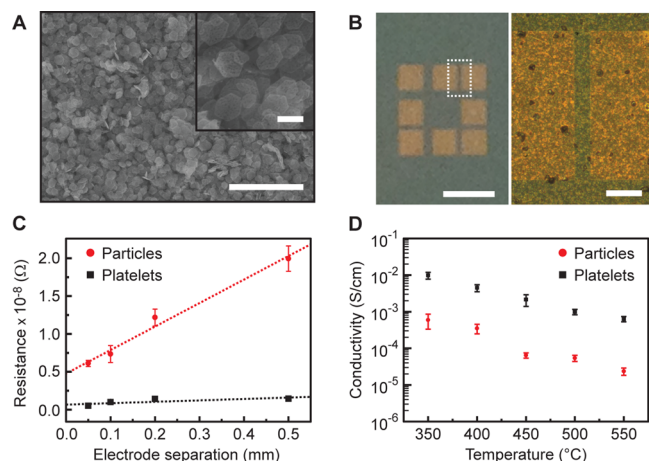


**Figure 4.** Electrical conductivity of NiO thin films. (A) SEM image of a nanoplatelet film calcined at 450 °C; scale bar, 1  $\mu\text{m}$ . (Inset) Higher resolution SEM image of the film; scale bar, 100 nm. (B) (Left) Optical image of microelectrodes patterned with  $500 \times 500 \mu\text{m}$  Au pads; scale bar, 1 mm. (Right) Bright-field optical microscopy image of the area denoted by the dashed box in the left-hand panel; scale bar, 100  $\mu\text{m}$ . (C) Typical microelectrode resistance measurements from 450 °C nanoparticle (red circles) and nanoplatelet (black squares) thin films. Lines represent linear fits to the data to determine conductivity values. (D) Conductivity of nanoparticle (red circles) and nanoplatelet (black squares) thin films as a function of the calcination/anneal temperature.

shown in Figure 4D. Under all conditions, nanoparticle films exhibit conductivities 10–100-fold smaller than nanoplatelet films.

In order to rule out a large disparity in the doping levels of nanoplatelets compared to nanoparticles, XPS spectra for both particles and platelets were collected in the O 1s region in order to quantify the Ni<sup>2+</sup> to Ni<sup>3+</sup> ratio (Figure 5A and Figure S5, Supporting Information). The peak at lower binding energy corresponds to octahedrally coordinated O<sup>2-</sup>, whereas the peak at higher binding energy corresponds to hydroxylated and/or defective NiO, i.e., Ni<sup>3+</sup> centers that act as the p-type dopant.<sup>29,33</sup> The ratio of the integrated peak areas was determined to be  $\sim 70:30$  for both nanoparticles and nanoplatelets at 450 °C (see Table S1, Supporting Information), suggesting that the doping level of the two materials is similar. UPS spectra of the particles and platelets (see Figure S6, Supporting Information) also show no appreciable difference in the Fermi level position relative to the valence band for the two materials, indicating the doping levels of the materials are approximately the same.

Additional measurements of the doping level were performed by Mott–Schottky analysis (see Figure S7, Supporting

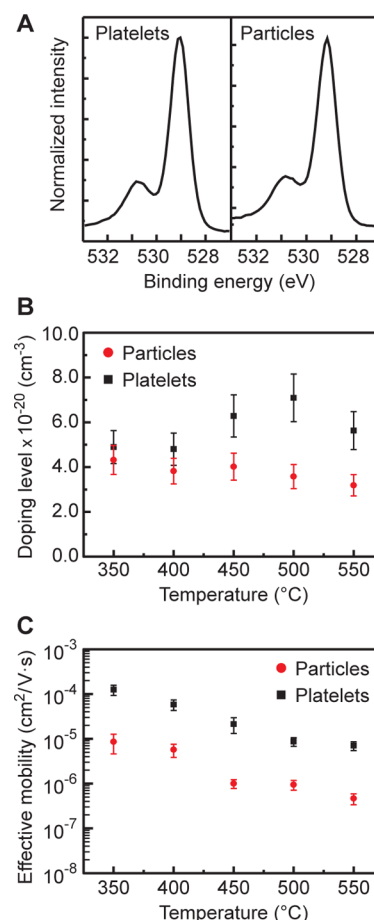


**Figure 5.** Doping level and effective mobility of NiO thin films. (A) XPS spectra in the O 1s region of nanoplatelets (left) and nanoparticle (right) thin films annealed at 450 °C. (B) Upper limit of doping level determined from Mott–Schottky analysis for nanoparticle (red circles) and nanoplatelet (black squares) thin films calcined at temperatures from 350 to 550 °C. (C) Lower limit of effective carrier mobility for nanoparticle (red circles) and nanoplatelets (black squares) thin films calcined at temperatures from 350 to 550 °C.

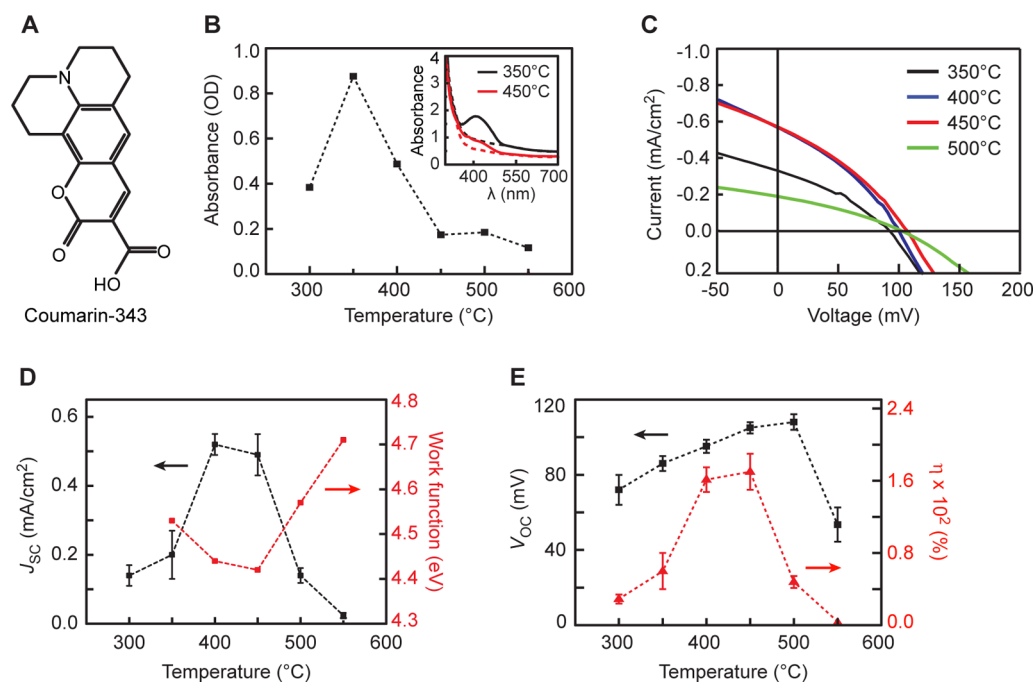


**Figure 6.** Photovoltaic performance of p-type DSSC devices using NiO nanoplatelets. (A) Molecular structure of the dye Coumarin-343. (B) Absorbance maxima for dyed thin films as a function of calcination temperature. Error bars are comparable in size to the marker symbols and omitted for clarity. (Inset) Absorption spectra for dyed (solid lines) and undyed (dashed lines) films of NiO calcined at 350 (black curves) and 450 °C (red curves). (C) Current density–voltage curves under simulated 1-sun illumination for DSSC devices fabricated with NiO calcination temperatures from 350 to 500 °C. (D)  $J_{sc}$  (black squares and left-hand axis) and work function from UPS data (red squares and right-hand axis) as a function of NiO calcination temperature. Error bars for the work function are comparable in size to the marker symbols and omitted for clarity. (E)  $V_{oc}$  (black squares and left-hand axis) and power-conversion efficiency ( $\eta$ ) (red triangles and right-hand axis) as a function of NiO calcination temperature.

Information) of nanoparticle and nanoplatelets films at multiple calcination temperatures. As shown in Figure 5B, the measurements yielded a doping level in the range from  $3 \times 10^{20}$  to  $7 \times 10^{20} \text{ cm}^{-3}$  for all samples. Note that because of ambiguities related to the film area, these values represent an upper limit on doping level (see Materials and Methods and Figure S7, Supporting Information), and actual values are likely to be substantially lower. Most importantly, analysis for particles and platelets yields similar results, confirming the similarity of the doping level for the two materials. Thus, we attribute the more than 10-fold increase in the conductivity of nanoplatelet films to an increase in the effective electrical mobility by a similar order of magnitude.

We determined an approximate lower limit on the mobility of NiO films, as shown in Figure 5C, utilizing the conductivities from microelectrode measurements and doping levels from Mott–Schottky analysis. For nanoparticle films annealed at 450 °C, a mobility value of  $\sim 1 \times 10^{-6} \text{ cm}^2/\text{V}\cdot\text{s}$  was determined, which is in good agreement with literature values ranging from  $\sim 5 \times 10^{-7}$  to  $\sim 6 \times 10^{-6} \text{ cm}^2/\text{V}\cdot\text{s}$ .<sup>18,21</sup> In comparison, the nanoplatelet film yielded a mobility value of  $\sim 2 \times 10^{-5} \text{ cm}^2/\text{V}\cdot\text{s}$ , which is more than 20-fold higher than the nanoparticle material. This substantial enhancement of the electrical mobility is consistent with the enhanced mobility observed for mesoscale  $\text{TiO}_2$  single crystals<sup>23</sup> and can be attributed to a reduction in carrier scattering and hopping at interparticle boundaries. Note that attempts to further confirm the higher effective mobility of nanoplatelet films using transient photoconductivity<sup>34</sup> were unsuccessful because the conductivity of the films did not change under high-intensity illumination (see Figure S8, Supporting Information). This observation is

consistent with the characteristically short lifetime of photo-injected holes in NiO.<sup>18,35</sup>

The data in Figure 5C show a progressively decreasing effective mobility with increasing temperature for both particles and platelet NiO. The mobility values change by  $\sim 1800\%$  from 350 to 550 °C. The similarity of the trend for both particles and platelets suggests that changes in the morphology of individual particles are not a primary cause of the reduced mobility. In addition, imaging of large areas of the thin-film materials (see Figure S4, Supporting Information) does not show any substantial change in the continuity of the thin films (e.g., cracks) that could easily explain the changes with temperature. Considering the change in film color (Figure 2B) yet negligible changes in doping level (Figure 5B), the dramatic change in mobility is best attributed to changes in the stoichiometry or chemistry of the NiO surface,<sup>18,36</sup> which could include migration of defect sites, dehydroxylation, and/or surface reconstruction that affect interparticle hopping and scattering. XPS data (see Figure S5 and Table S1, Supporting Information) show progressively decreasing signals from hydroxylated/defective NiO with increasing anneal temperature, suggesting a noteworthy change in the composition of the material with temperature. Nevertheless, the reduced mobility of NiO at higher calcination or annealing temperatures is a relatively surprising outcome that will be the subject of future theoretical and experimental investigations.

To delineate the effect of the improved electrical mobility and hierarchical platelet/pore morphology on p-type DSSC performance, we fabricated devices following standard procedures using the Coumarin-343 dye (Figure 6A) and iodide/tri-iodide electrolyte with a low tri-iodide concentration, which avoids substantial photocurrent generation by direct

photoexcitation of the electrolyte.<sup>36–38</sup> Note that Coumarin-343, although not an optimal chromophore for NiO in comparison to donor–acceptor dyes,<sup>14–17</sup> is the most widely reported chromophore for NiO<sup>39</sup> and thus a good benchmark to elucidate trends in the DSSC performance.

To quantify dye loading on the NiO films, absorption spectra were acquired as a function of calcination temperature (see Figure 6B and Figure S9, Supporting Information). Spectra show a 4-fold decrease in dye loading from 350 to 450 °C. Measurements of the film surface area using BET analysis (see Figure S10, Supporting Information) showed a similar linear decrease in surface area over the same temperature range. Thus, the decreasing dye absorption appears to be correlated with the loss of surface area associated with a morphological change from high density of small pores to low density of large pores.

The photovoltaic performance of NiO devices calcined at temperatures from 300 to 550 °C is summarized in Figure 6C–E. As apparent from current density–voltage curves under 1-sun illumination (Figure 6C), the highest performance was observed for samples calcined at 400 and 450 °C. Most importantly, a nanoplatelet device fabricated at 450 °C yielded a power-conversion efficiency ~30% higher, on average (see Table 1), than the comparable devices fabricated with commercial nanoparticles under identical conditions and with identical dye loading (see Figure S9, Supporting Information).

The DSSC performance of the platelets shows distinct trends as a function of calcination temperature. The short-circuit current density ( $J_{SC}$ ) from the devices (Figure 6D) maximizes at 400–450 °C and is several times lower at both 350 and 500 °C. Interestingly, the maxima in absorption and  $J_{SC}$  do not occur at the same temperature but rather at 350 and 400 °C, respectively. The increasing  $J_{SC}$  despite decreasing absorption suggests that the internal quantum efficiency (IQE) of the DSSC devices substantially increases in the 400–450 °C temperature range. As shown in Figure 6D, UPS was used to determine the work function of NiO as a function of temperature (see Figure S11, Supporting Information, for spectra). For p-type devices that inject a hole into the semiconductor material, a lower work function increases the driving force for charge injection; thus, a higher IQE would be expected. The work function first decreases and then increases with temperature, reaching the lowest values at 400 and 450 °C. The trend is well correlated with the changes in  $J_{SC}$ , suggesting that the lower work function does serve to increase the charge injection efficiency and thus IQE and  $J_{SC}$  of the DSSC devices.

Although the  $J_{SC}$ , dye loading, and film thicknesses of nanoplatelet and nanoparticle devices optimized at 450 °C are nearly identical, the open-circuit voltage ( $V_{OC}$ ) values of nanoplatelet devices (see Table 1) are 15–20% higher, on average, than nanoparticle devices. We attribute the improved

$V_{OC}$  to reduced recombination as a result of faster hole diffusion through the mesoporous nanoplatelet film. In addition, the  $V_{OC}$  of the nanoplatelet devices increases linearly with calcination temperature (Figure 6E), reaching a maximum of  $108 \pm 4$  mV at 500 °C. At temperatures of 550 °C and above, we observed decreasing mechanical stability of the NiO films, which lowered the photovoltaic metrics of these and all higher temperature devices. The combination of trends with  $J_{SC}$  and  $V_{OC}$  produced the maximum power-conversion efficiency for nanoplatelet DSSC devices (see Figure 6E and Table 1) at a calcination temperature of 450 °C.

## 4. CONCLUSIONS

We developed a method to synthesize high-quality NiO with a unique hierarchical structure composed of ultrathin, two-dimensional hexagonal platelets perforated with a high density of nanoscale pores. We observed a more than 10-fold improvement in the electrical mobility of thin films of this material in comparison to films of conventional nanoparticles. p-Type DSSC devices fabricated with the platelets exhibited a modest, 20–30% increase in performance over similar nanoparticle devices. Results collected over a range of calcination temperatures suggest that 450 °C is an optimal temperature for preparation of NiO nanoplatelets that have high mobility, surface area, and charge injection efficiency. In conjunction with efforts to optimize chromophores for NiO,<sup>14–17</sup> the capability to rationally control the size, morphology, crystallinity, and electrical mobility of this material should provide a route to further improve the performance for tandem DSSC and DSPEC solar energy devices.

## ■ ASSOCIATED CONTENT

### ● Supporting Information

Figures containing XRD, XPS, and UPS data, Debye–Scherrer analysis, photoconductivity measurements, UV–vis absorption spectra, Mott–Schottky analysis, and BET surface area measurements. This material is available free of charge via the Internet at <http://pubs.acs.org>.

## ■ AUTHOR INFORMATION

### Corresponding Author

\*E-mail: [jfcahoon@unc.edu](mailto:jfcahoon@unc.edu).

### Author Contributions

The manuscript was written through contributions of all authors. All authors have given approval to the final version of the manuscript.

### Notes

The authors declare no competing financial interest.

## ■ ACKNOWLEDGMENTS

This work was wholly funded by the UNC Energy Frontier Research Center (EFRC) “Center for Solar Fuels”, an EFRC funded by the U.S. Department of Energy, Office of Science, Office of Basic Energy Sciences, under Award DE-SC0001011. E.E.O. acknowledges the J. Thurman Freeze Summer Research Scholarship. We thank A. Kumbhar of CHANL for assistance with TEM imaging.

## ■ REFERENCES

- (1) Yella, A.; Lee, H. W.; Tsao, H. N.; Yi, C. Y.; Chandiran, A. K.; Nazeeruddin, M. K.; Diau, E. W. G.; Yeh, C. Y.; Zakeeruddin, S. M.; Gratzel, M. Porphyrin-Sensitized Solar Cells with Cobalt (II/III)-

**Table 1. Photovoltaic Metrics for NiO DSSC Devices Using Hexagonal Platelets or Spherical Particles**

	$V_{OC}$ (mV)	$J_{SC}$ (mA/cm <sup>2</sup> )	FF (%)	$\eta$ (%)
platelet <sup>a,b</sup>	106 ± 3	0.48 ± 0.03	32.5 ± 0.4	0.017 ± 0.001
particle <sup>a,b</sup>	90 ± 10	0.47 ± 0.06	31 ± 2	0.013 ± 0.003
platelet <sup>a,c</sup>	104–108	0.43–0.52	31.6–32.9	0.014–0.018
particle <sup>a,c</sup>	65–96	0.43–0.50	27–32	0.007–0.016

<sup>a</sup>For a calcination/anneal temperature of 450 °C. <sup>b</sup>Average from 8 devices. <sup>c</sup>Performance range from worst to champion device as defined by lowest and highest  $\eta$ .



Based Redox Electrolyte Exceed 12% Efficiency. *Science* **2011**, *334*, 629–634.

(2) Alibabaei, L.; Luo, H.; House, R. L.; Hoertz, P. G.; Lopez, R.; Meyer, T. J. Applications of Metal Oxide Materials in Dye Sensitized Photoelectrosynthesis Cells for Making Solar Fuels: Let the Molecules do the Work. *J. Mater. Chem. A* **2013**, *1*, 4133–4145.

(3) Alibabaei, L.; Brennaman, M. K.; Norris, M. R.; Kalanyan, B.; Song, W.; Losego, M. D.; Concepcion, J. J.; Binstead, R. A.; Parsons, G. N.; Meyer, T. J. Solar Water Splitting in a Molecular Photoelectrochemical Cell. *Proc. Natl. Acad. Sci. U.S.A.* DOI: 10.1073/pnas.1319628110.

(4) Concepcion, J. J.; House, R. L.; Papanikolas, J. M.; Meyer, T. J. Chemical Approaches to Artificial Photosynthesis. *Proc. Natl. Acad. Sci. U.S.A.* **2012**, *109*, 15560–15564.

(5) Odobel, F.; Pellegrin, Y. Recent Advances in the Sensitization of Wide-Band-Gap Nanostructured p-Type Semiconductors. Photo-voltaic and Photocatalytic Applications. *J. Phys. Chem. Lett.* **2013**, *4*, 2551–2564.

(6) Nozik, A. J. Photochemical Diodes. *Appl. Phys. Lett.* **1977**, *30*, 567–569.

(7) He, J. J.; Lindstrom, H.; Hagfeldt, A.; Lindquist, S. E. Dye-Sensitized Nanostructured Tandem Cell-First Demonstrated Cell with a Dye-Sensitized Photocathode. *Sol. Energy Mater. Sol. Cells* **2000**, *62*, 265–273.

(8) Nattestad, A.; Mozer, A. J.; Fischer, M. K. R.; Cheng, Y. B.; Mishra, A.; Bauerle, P.; Bach, U. Highly Efficient Photocathodes for Dye-Sensitized Tandem Solar Cells. *Nat. Mater.* **2010**, *9*, 31–35.

(9) Nattestad, A.; Zhang, X. L.; Bach, U.; Cheng, Y. B. Dye-Sensitized CuAlO<sub>2</sub> Photocathodes for Tandem Solar Cell Applications. *J. Photonics Energy* **2011**, *1*, 011103.

(10) Yu, M. Z.; Natu, G.; Ji, Z. Q.; Wu, Y. Y. p-Type Dye-Sensitized Solar Cells Based on Delafossite CuGaO<sub>2</sub> Nanoplates with Saturation Photovoltages Exceeding 460 mV. *J. Phys. Chem. Lett.* **2012**, *3*, 1074–1078.

(11) Xu, X.; Zhang, B.; Cui, J.; Xiong, D.; Shen, Y.; Chen, W.; Sun, L.; Cheng, Y.; Wang, M. Efficient p-Type Dye-Sensitized Solar Cells Based on Disulfide/Thiolate Electrolytes. *Nanoscale* **2013**, *5*, 7963–7969.

(12) Yu, M.; Draskovic, T. I.; Wu, Y. Cu(I)-Based Delafossite Compounds as Photocathodes in p-Type Dye-Sensitized Solar Cells. *Phys. Chem. Chem. Phys.* **2014**, *16*, 5026–5033.

(13) Powar, S.; Daeneke, T.; Ma, M. T.; Fu, D.; Duffy, N. W.; Götz, G.; Weideler, M.; Mishra, A.; Bäuerle, P.; Spiccia, L.; et al. Highly Efficient p-Type Dye-Sensitized Solar Cells based on Tris(1,2-diaminoethane)Cobalt(II)/(III) Electrolytes. *Angew. Chem., Int. Ed.* **2013**, *52*, 602–605.

(14) Le Pleux, L.; Smeigh, A. L.; Gibson, E.; Pellegrin, Y.; Blart, E.; Boschloo, G.; Hagfeldt, A.; Hammarström, L.; Odobel, F. Synthesis, Photophysical and Photovoltaic Investigations of Acceptor-Functionalized Perylene Monoimide Dyes for Nickel Oxide p-Type Dye-Sensitized Solar Cells. *Energy Environ. Sci.* **2011**, *4*, 2075–2084.

(15) Zhang, X. L.; Huang, F. Z.; Nattestad, A.; Wang, K.; Fu, D. C.; Mishra, A.; Bauerle, P.; Bach, U.; Cheng, Y. B. Enhanced Open-Circuit Voltage of p-Type DSC with Highly Crystalline NiO Nanoparticles. *Chem. Commun.* **2011**, *47*, 4808–4810.

(16) Zhang, X. L.; Zhang, Z.; Chen, D.; Bauerle, P.; Bach, U.; Cheng, Y. B. Sensitization of Nickel Oxide: Improved Carrier Lifetime and Charge Collection by Tuning Nanoscale Crystallinity. *Chem. Commun.* **2012**, *48*, 9885–9887.

(17) Ji, Z.; Natu, G.; Wu, Y. Cyclometalated Ruthenium Sensitizers Bearing a Triphenylamino Group for p-Type NiO Dye-Sensitized Solar Cells. *ACS Appl. Mater. Interfaces* **2013**, *5*, 8641–8648.

(18) Odobel, F.; Pellegrin, Y.; Gibson, E. A.; Hagfeldt, A.; Smeigh, A. L.; Hammarström, L. Recent Advances and Future Directions to Optimize the Performances of p-Type Dye-Sensitized Solar Cells. *Coord. Chem. Rev.* **2012**, *256*, 2414–2423.

(19) Huang, Z.; Natu, G.; Ji, Z.; He, M.; Yu, M.; Wu, Y. Probing the Low Fill Factor of NiO p-Type Dye-Sensitized Solar Cells. *J. Phys. Chem. C* **2012**, *116*, 26239–26246.

(20) Osburn, C. M.; Vest, R. W. Defect Structure and Electrical Properties of NiO. 1. High Temperature. *J. Phys. Chem. Solids* **1971**, *32*, 1331–1342.

(21) Note that ref 18 reports diffusion constants,  $D$ , of  $1.3 \times 10^{-8}$ ,  $4.0 \times 10^{-8}$ , and  $1.6 \times 10^{-7}$  cm<sup>2</sup>/s for NiO mesoporous films. These values were converted to mobilities,  $\mu$ , of  $5.1 \times 10^{-7}$ ,  $1.6 \times 10^{-6}$ , and  $6.2 \times 10^{-6}$  cm<sup>2</sup>/V·s, respectively, using the Einstein relation  $\mu = qD/k_B T$ , where  $q$  is the elementary charge,  $k_B$  is the Boltzmann constant, and  $T$  is temperature, assumed to be 25 °C.

(22) Law, M.; Greene, L. E.; Johnson, J. C.; Saykally, R.; Yang, P. Nanowire Dye-Sensitized Solar Cells. *Nat. Mater.* **2005**, *4*, 455–459.

(23) Crossland, E. J. W.; Noel, N.; Sivaram, V.; Leijtens, T.; Alexander-Webber, J. A.; Snaith, H. J. Mesoporous TiO<sub>2</sub> Single Crystals Delivering Enhanced Mobility and Optoelectronic Device Performance. *Nature* **2013**, *495*, 215–219.

(24) Warren, S. C.; Voitchovsky, K.; Dotan, H.; Leroy, C. M.; Cornuz, M.; Stellacci, F.; Hébert, C.; Rothschild, A.; Grätzel, M. Identifying Champion Nanostructures for Solar Water-Splitting. *Nat. Mater.* **2013**, *12*, 842–849.

(25) Durand-Keklikian, L.; Haq, I.; Matijevic, E. Preparation and Characterization of Well-Defined Colloidal Nickel Compounds. *Colloids Surf., A* **1994**, *92*, 267–275.

(26) Behm, N.; Brokaw, D.; Overson, C.; Peloquin, D.; Poler, J. C. High-Throughput Microwave Synthesis and Characterization of NiO Nanoplates for Supercapacitor Devices. *J. Mater. Sci.* **2013**, *48*, 1711–1716.

(27) Striemer, C. C.; Gaborski, T. R.; McGrath, J. L.; Fauchet, P. M. Charge- and Size-Based Separation of Macromolecules using Ultrathin Silicon Membranes. *Nature* **2007**, *445*, 749–753.

(28) Monk, P.; Mortimer, R.; Rosseinsky, D. *Electrochromism and Electrochromic Devices*; Cambridge University Press: Cambridge, 2007.

(29) Manders, J. R.; Tsang, S.-W.; Hartel, M. J.; Lai, T.-H.; Chen, S.; Amb, C. M.; Reynolds, J. R.; So, F. Solution-Processed Nickel Oxide Hole Transport Layers in High Efficiency Polymer Photovoltaic Cells. *Adv. Funct. Mater.* **2013**, *23*, 2993–3001.

(30) Renaud, A.; Chavillon, B.; Cario, L.; Pleux, L. L.; Szuwarski, N.; Pellegrin, Y.; Blart, E.; Gautron, E.; Odobel, F.; Jobic, S. Origin of the Black Color of NiO Used as Photocathode in p-Type Dye-Sensitized Solar Cells. *J. Phys. Chem. C* **2013**, *117*, 22478–22483.

(31) Cattaneo, E.; Reigel, B., Chemistry, Electrochemistry, and Electrochemical Applications | Nickel. In *Encyclopedia of Electrochemical Power Sources*; Garche, J., Ed.; Elsevier: Amsterdam, 2009; pp 769–809.

(32) Brown, A. B. D.; Clarke, S. M.; Rennie, A. R. Ordered Phase of Platelike Particles in Concentrated Dispersions. *Langmuir* **1998**, *14*, 3129–3132.

(33) Ratcliff, E. L.; Meyer, J.; Steirer, K. X.; Garcia, A.; Berry, J. J.; Ginley, D. S.; Olson, D. C.; Kahn, A.; Armstrong, N. R. Evidence for Near-Surface NiOOH Species in Solution-Processed NiO<sub>x</sub> Selective Interlayer Materials: Impact on Energetics and the Performance of Polymer Bulk Heterojunction Photovoltaics. *Chem. Mater.* **2011**, *23*, 4988–5000.

(34) Snaith, H. J.; Grätzel, M. Electron and Hole Transport through Mesoporous TiO<sub>2</sub> Infiltrated with Spiro-MeOTAD. *Adv. Mater.* **2007**, *19*, 3643–3647.

(35) Morandeira, A.; Boschloo, G.; Hagfeldt, A.; Hammarström, L. Photoinduced Ultrafast Dynamics of Coumarin 343 Sensitized p-Type-Nanostructured NiO Films. *J. Phys. Chem. B* **2005**, *109*, 19403–19410.

(36) Zhu, H.; Hagfeldt, A.; Boschloo, G. Photoelectrochemistry of Mesoporous NiO Electrodes in Iodide/Triiodide Electrolytes. *J. Phys. Chem. C* **2007**, *111*, 17455–17458.

(37) Qin, P.; Zhu, H.; Edvinsson, T.; Boschloo, G.; Hagfeldt, A.; Sun, L. Design of an Organic Chromophore for P-Type Dye-Sensitized Solar Cells. *J. Am. Chem. Soc.* **2008**, *130*, 8570–8571.

(38) Nattestad, A.; Ferguson, M.; Kerr, R.; Cheng, Y. B.; Bach, U. Dye-Sensitized Nickel(II) Oxide Photocathodes for Tandem Solar Cell Applications. *Nanotechnol.* **2008**, *19*, 295304.

(39) Odobel, F.; Le Pleux, L. c.; Pellegrin, Y.; Blart, E. New Photovoltaic Devices Based on the Sensitization of p-type Semiconductors: Challenges and Opportunities. *Acc. Chem. Res.* **2010**, *43*, 1063–1071.